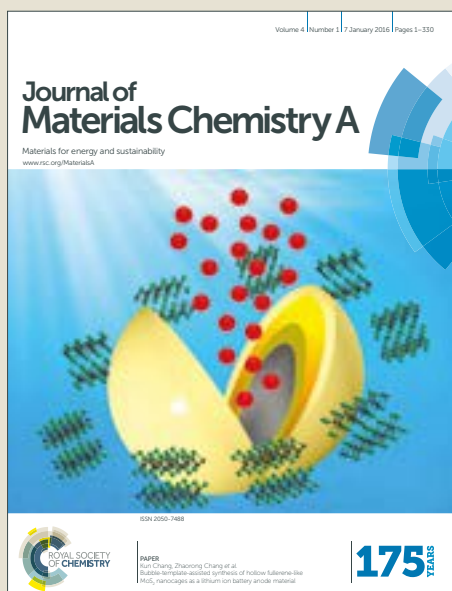


Journal of Materials Chemistry A

Accepted Manuscript

This article can be cited before page numbers have been issued, to do this please use: L. Dai, X. Wang, S. Yang, T. Zhang, P. ren, J. Ye, B. Nan, X. Wen, Z. Zhou, R. Si, C. Yan and Y. Zhang, *J. Mater. Chem. A*, 2018, DOI: 10.1039/C8TA03320J.



This is an Accepted Manuscript, which has been through the Royal Society of Chemistry peer review process and has been accepted for publication.

Accepted Manuscripts are published online shortly after acceptance, before technical editing, formatting and proof reading. Using this free service, authors can make their results available to the community, in citable form, before we publish the edited article. We will replace this Accepted Manuscript with the edited and formatted Advance Article as soon as it is available.

You can find more information about Accepted Manuscripts in the [author guidelines](#).

Please note that technical editing may introduce minor changes to the text and/or graphics, which may alter content. The journal's standard [Terms & Conditions](#) and the ethical guidelines, outlined in our [author and reviewer resource centre](#), still apply. In no event shall the Royal Society of Chemistry be held responsible for any errors or omissions in this Accepted Manuscript or any consequences arising from the use of any information it contains.

ARTICLE

Intrinsic composition and electronic effects of multicomponent platinum nanocatalysts with high activity and selectivity for ethanol oxidation reaction

Lin-Xiu Dai,^{‡a} Xin-Yu Wang,^{‡a} Sheng-Song Yang,^{‡a} Tao Zhang,^a Peng-Ju Ren,^b Jin-Yu Ye,^c Bing Nan,^d Xiao-Dong Wen,^{*b} Zhi-You Zhou,^{*c} Rui Si,^d Chun-Hua Yan,^a Ya-Wen Zhang^{*a}

Received 00th January 20xx,
Accepted 00th January 20xx

DOI: 10.1039/x0xx00000x

www.rsc.org/

The sluggish kinetics of ethanol oxidation reaction (EOR) challenges us to design and synthesize high-performance multicomponent nanocatalysts. Herein, we report the intrinsic composition and electronic effects for achieving the enhanced catalytic performances towards EOR by the combination of experiments and density functional theory (DFT) computations. Late 3d transition metals and main group (IIIA and IVA) metals were introduced to construct ternary Pt₃RhM (M = Fe, Co, Ni, Cu; Ga, In, Sn, Pb) nanoalloys with a similar geometric structure (nearly spherical) and crystallize size (ca. 8.5 nm) by one-pot solvothermal method. The main group metals outperform the transition metals in the enhancement of the EOR activity and CO₂ selectivity. Especially, Pt₃RhSn/C exhibits 67- and 7-fold enhancements of the specific activity and mass activity at 0.45 V (vs RHE) for EOR in acidic condition, compared with the commercial Pt/C catalyst. The trends in catalytic activity were explained by DFT calculations which established a volcano-shaped relationship between the EOR activity and the sum of the oxygen and carbon binding energies (E_O+E_C). Among above catalysts, the state-of-the-art Pt₃RhSn/C catalyst wins in an optimum E_O+E_C value with a moderate adsorption strength of stable intermediates. In addition, the CO₂ selectivity is linearly correlated with the sum of oxygen and H₂O binding energies (E_O+E_{H2O}), which matches well with the experimental results of typical catalysts. Therefore, the E_O+E_C and E_O+E_{H2O} were creatively served as the activity and selectivity descriptors to rationalize and predict these chemical trends presented in the experiments of nanoalloys catalyzed EOR. The revealed concept that the composition-performance relationship origins from the synergistic electronic effect of the nanoalloys, promises an alternative strategy for developing novel solid catalysts towards EOR.

^a Beijing National Laboratory for Molecular Sciences, College of Chemistry and Molecular Engineering, Peking University, Beijing 100871, China.

^b State Key Laboratory of Coal Conversion, Institute of Coal Chemistry, Chinese Academy of Sciences, Taiyuan, Shanxi 030001, China & National Energy Center for Coal to Clean Fuels, Synfuels China Co., Ltd, Huairou District, Beijing, 101400, China.

^c State Key Laboratory of Physical Chemistry of Solid Surfaces, Department of Chemistry, College of Chemistry and Chemical Engineering, Xiamen University, Xiamen 361005, China.

^d Shanghai Synchrotron Radiation Facility, Shanghai Institute of Applied Physics, Chinese Academy of Sciences, Shanghai 201204, China.

[‡] These authors contribute equally.

*Email - ywzhang@pku.edu.cn

Electronic Supplementary Information (ESI) available: [details of any supplementary information available should be included here]. See DOI: 10.1039/x0xx00000x

Introduction

Direct ethanol fuel cells (DEFCs) have tremendous potentials in energy conservation and sustainable energy system because of their high energy density, easy storage and transportation, and low environmental impact.¹⁻³ However, sluggish kinetics of anode reaction, and poor performance (activity, selectivity and durability) of the catalysts impede the development of DEFCs.⁴ For ethanol electro-oxidation reaction (EOR), the evolution of catalysts from single metal (Pt)⁶ to binary Pt-based catalysts⁷⁻⁸ to ternary Pt-based catalysts,⁹⁻¹⁵ demonstrates that multiple active sites are required to work synergistically for different elementary steps of EOR. Generally, the additive active sites to Pt surface help to address two central challenges in EOR: C-C cleavage for high selectivity to CO₂ product (Rh or Ir sites)^{16, 17} and the removing of C1 intermediates for high activity.^{18, 19}

Nørskov et al. put forward the design approach of solid catalysts through tailoring the electronic structure by means of changing composition and atomic arrangement.²⁰ The combination of theoretical calculations and experiments has been implemented to elucidate the composition-performance relationship on mono- and bi-metallic surfaces for hydrogen evolution/oxidation reactions (HER/HOR) and oxygen evolution/reduction reactions (OER/ORR) with limited intermediates.²¹⁻²³ For alcohol oxidation reactions (AORs), methanol electro-oxidation reaction (MOR) is the most investigated one. Composition-dependent linear energy relations and volcano-shape curves with different descriptors for mono- and bi-metals have been discovered.²⁴⁻²⁶ However, there are few investigations on electronic effects of bimetallic and trimetallic catalysts in more complicated EOR, probably because it is difficult to find effective descriptors to correlate the selectivity and activity.²⁷⁻³² As the composition-performance relationship of the state-of-the-art ternary catalysts plays important roles in screening highly efficient EOR catalysts, simple and universal synthetic methods as well as proper descriptors are required for deepening the understanding of catalytic mechanism.³³⁻³⁷

Developing controllable synthetic method of ternary EOR catalysts benefits the composition effect researches with other structure factors of catalysts excluded, and the effective construction of high-performance EOR catalysts screened by theoretic and experimental predictions. However, the colloidal synthetic technology of multi-component nanocatalysts is not as mature as that of mono- and bi-metallic nanocatalysts. Hence, the controllable synthesis of three-component nanocatalysts together with the investigation of their synergistic electronic effects on EOR performance are urgent to be addressed.

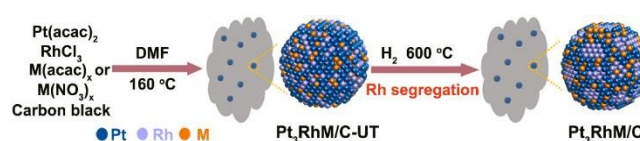
In this work, a set of earth-abundant elements of IIIA and IVA metals (Ga, In, Sn, Pb), and late 3d transition metals (Fe, Co, Ni, Cu) are employed to partially substitute noble metals of Pt and Rh by constructing Pt-Rh-M nanoalloys, and to uncover the roles of electronic perturbation in their EOR reactivity. Pt₃RhM/C nanocatalysts with a similar geometric structure (nearly spherical) and crystallize size (ca. 8.5 nm) were

controllably synthesized. Electrochemical measurements and *in situ* Fourier transform infrared spectroscopy (FTIR) indicate that main group metals display better promotion effect on EOR activity and selectivity at low potential. DFT calculations demonstrate the respective activity and selectivity descriptors, which rationalize these chemical trends of Pt₃RhM/C catalysts in EOR performance, aroused from the modulation of surface electronic structures with alternative components.

Result and discussion

Synthesis, characterization and EOR measurements

To investigate the composition-reactivity relationship, we prepared highly efficient Pt₃RhM/C catalysts with comparable structures. Highly dispersed Pt₃RhM/C (M = Ga, In, Sn, Pb; Fe, Co, Ni, Cu) nanocatalysts were synthesized using N, N-dimethylformamide (DMF) as the solvent and reductant, carbon black as support, following by H₂ thermal treatment (Scheme 1). The atomic ratio of Pt to Rh is set to 3:1 according to literature report,^{11, 38} the M content with 20% of the total atoms depends on the highest EOR performance (see Electronic Supplementary Information, Figure S1). As shown in Figure 1A and Figure S2-S3, all Pt₃RhM/C catalysts show spherical shape with an average diameter of ca. 8.5 nm. High-angle annular dark-field scanning transmission electron microscopy (HAADF-STEM) EDS line and mapping scans demonstrate that the Pt₃RhM/C catalysts share similar element distributions. Powder X-ray diffraction (PXRD) patterns of Pt₃RhM/C (Figure S4) are assigned to fcc-structured alloy, the main peaks show regularly shift due to the difference in the atomic radius of M. As shown in Table S1, the crystallite size of Pt₃RhM/C was calculated based on Scherrer formula, which is close to the statistic particle diameter from TEM images (Table S2). The lattice parameters of Pt₃RhM/C were also calculated and listed in Table S1, which reflect the bulk lattice compression and expansion with the additive M. For example, the (111) peak of Pt₃RhSn/C nanocrystals shifts negatively compared with that of Pt₃Rh/C, which evidences alloy formation and bulk lattice expansion (2%) compared with Pt₃Rh alloy. Phase segregation of Pt₃RhPb/C nanocrystals is observed. The major peaks of Pt₃RhPb/C nanocrystals are attributed to the Rh-doped Pt₃Pb intermetallic phase, which are 0.3 degree higher than Pt₃Pb intermetallic phase (Pt₃Pb, JCPDS: 00-006-0574). The trace impurity peaks are ascribed to the segregation of Pt₃Rh on the surface.³⁹ Inductively coupled plasma atomic emission spectroscopy (ICP-AES) data display the overall atomic ratios of about 3:1:1 (Pt:Rh:M) for all catalysts, X-ray photoelectron spectroscopy (XPS) analyses reveal slight enrichment of the Rh component on the surface (Table S2). Hence, DMF solvothermal method is a relatively universal route to prepare Pt₃RhM/C catalysts. The EOR performances of these catalysts could reflect their composition-reactivity relationship with negligible differences in their structures.



Scheme 1. The schematic illustration of the fabrication of highly dispersive Pt₃RhM/C catalysts.

To examine the EOR activity and stability of the Pt₃RhM/C catalysts, linear sweep voltammograms (LSVs)^{9, 11} at a sweep rate of 1 mV s⁻¹ and potentiostatic chronoamperometric (CA) experiments in 0.5 M CH₃CH₂OH / 0.1 M HClO₄ were performed (Figure S5). As the ideal catalysts should have higher current density at lower potential, we choose 0.45 V for comparison in terms of technique interest.¹² High Stable cyclic voltammograms (CVs) in 0.1 M HClO₄ were utilized to determine the electrochemically accessible surface area (ECSA), because the H-adsorption method has been widely applied in the measurement of ECSA of Pt-Rh-Sn electrode, and CO stripping is not a reasonable one.^{12, 13, 40} All potentials mentioned are relative to the reversible hydrogen electrode (RHE), the reference electrode had been calibrated by using reversible hydrogen electrode. The specific activity of Pt₃Rh and Pt₃RhM/C (M = Fe, Co, Ni, Cu; Ga, In, Sn, Pb) at 0.45 V extracted from LSV curves, follows a sequence that Pt₃RhSn/C > Pt₃RhIn/C > Pt₃RhGa/C > Pt₃RhPb/C > Pt₃RhCu/C > Pt₃RhCo/C > Pt₃RhNi/C > Pt₃RhFe/C > Pt₃Rh/C > Pt/C (ca. 3.5 nm in size), which suggests that the promotion effect of main group metals outperformed that of transition metals (Figure 1B and Table S3). Clearly, the EOR performance of the Pt₃RhSn/C catalyst is dramatically superior to the commercial Pt/C catalysts (Figure 1C). Its specific activity of 0.0919 mA cm⁻² and mass activity of 23.4 mA mg_{Pt}⁻¹, are 67- and 7-fold enhancements compared with the commercial Pt/C catalyst at 0.45 V. The specific activities of Pt₃RhSn/C at 0.50 V and 0.55 V are 42 and 22 times higher than that of Pt/C. In addition, Pt₃RhSn/C catalyst also has better EOR activity than the synthesized Pt₃Sn/C catalyst (Figure S6), proving the necessity of incorporating multiply active sites in the catalysts. Surprisingly, after 10 h CA test, Pt₃RhSn/C catalyst shows high electrochemical durability (Figure 1D).

In order to compare with the previous literature reports in the same test conditions (0.5 M CH₃CH₂OH / 0.1 M HClO₄ solution), the EOR activities of the state-of-the-art catalysts at different sweep rates based on reported data are listed in Table S4.^{9, 13, 14} The mass activity of Pt₃RhSn/C at high scan rates and the specific activity at quasi-steady-state scan rate are superior to the other reported catalysts. As the elemental distributions of three metals on surface and bulk are very different, more Pt and Rh sites are exposed on the Pt₃RhSn/C surface. In addition, the types of active sites (Pd, Ni and Sn) and catalysts (alloyed and supported) may influence the reaction path, resulting in different EOR performance. After LSV and CA tests, a small amount of Rh and M atoms were slightly leached. The diameter and atomic ratios of Pt to Rh to M of the Pt₃RhM/C nanocatalysts detected by ICP-AES are listed in Table S5. In addition, no obvious change in size, shape and dispersion of these catalysts after electrochemical tests was observed (Figure S7).

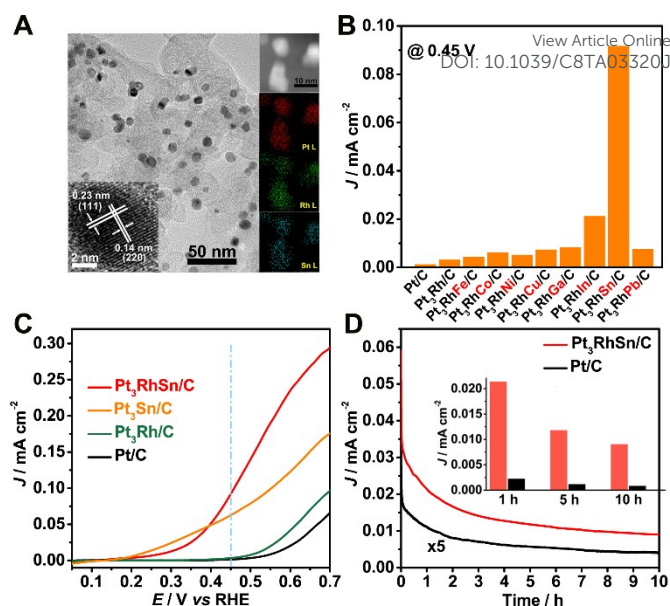


Figure 1. (A) Transmission electron microscope (TEM) image, high-resolution transmission electron microscope (HRTEM) image (inset in left bottom) and HAADF-STEM-EDS mapping scans (right side) of Pt₃RhSn/C catalyst. (B) Summary of current densities of Pt₃RhM/C catalysts extracted from LSV curves recorded at 0.45 V. (C) LSVs curves of Pt₃RhSn/C, Pt₃Sn/C, Pt₃Rh/C and Pt/C at a sweep rate of 1 mV s⁻¹. (D) CA curves of Pt₃RhSn/C and Pt/C at 0.45 V, the current density of Pt/C was magnified five times. B, C and D were measured in 0.5 M CH₃CH₂OH/0.1 M HClO₄ solution, the current densities were normalized by ECSA.

In situ Fourier transform infrared spectroscopy (FTIR) characterizations

In situ FTIR was used to identify the intermediates and products of ethanol oxidation. Pt₃RhSn/C, Pt₃RhCo/C, Pt₃Rh/C and Pt/C catalysts were typically selected to verify the possible intrinsic mechanism and product selectivity by sweeping the potential from 0.15 V to 0.95 V (Figure 2A-D). All the assignments of the characteristic bands are listed in Table S6 according to previous reports.^{19, 41} The signature peak of CO₂ (~2343 cm⁻¹) corresponds to complete oxidation of ethanol, indicating the breakage of the C-C bond in ethanol. The obvious CO₂ peaks were first observed on Pt₃RhSn/C, followed by Pt₃RhCo/C, Pt₃Rh/C and Pt/C. It implies that Pt₃RhSn/C possesses the capability to fully oxidize ethanol at extremely low potential. The bipolar peak at 2047 cm⁻¹ was assigned to linearly absorbed CO (CO_L). Stronger bounded CO_L was observed at much lower potential (0.25 V) on Pt/C compared with its apparent peak potential of CO₂ (0.65 V), implying insufficient oxidation of CO on Pt/C at low potential. No CO_L peak was observed on Pt₃RhSn/C, suggesting CO_L adsorption was weakened by optimized electronic structure of Pt₃RhSn/C. The band located at around 1718 cm⁻¹ attributed to the stretch vibration of the C=O bond in acetaldehyde and/or acetic acid, both of which are partial oxidation products. The C-O stretching at 1285 cm⁻¹ and C-H stretching at 1353 cm⁻¹ are characteristic absorption bands of acetic acid. The onset potentials of obvious vibration peaks of C=O, C-H and C-O

bonds follow a sequence: $\text{Pt}_3\text{RhSn/C} > \text{Pt}_3\text{RhCo/C} \approx \text{Pt}_3\text{Rh/C} > \text{Pt/C}$, confirming that the addition of Rh and M significantly decrease the yield of acetaldehyde and/or acetic acid. The band intensities are extracted as a function of potential (Figure S8). It should be mentioned that the comparison of real Faradaic selectivity requires external calibration.⁴² Herein, we only calculated the relative peak intensity to roughly estimate the product selectivity.⁹ As shown in Figure 2E, the ratio of $\text{CO}_2/\text{CH}_3\text{COOH}$ is higher on $\text{Pt}_3\text{RhSn/C}$ and $\text{Pt}_3\text{RhCo/C}$, indicating that the formation of acetic acid is dramatically inhibited on $\text{Pt}_3\text{RhM/C}$ catalysts. Especially, $\text{Pt}_3\text{RhSn/C}$ displays the highest CO_2 selectivity. Therefore, it could be concluded that the addition of main group metals improves the CO_2 selectivity more than that of transition metals.

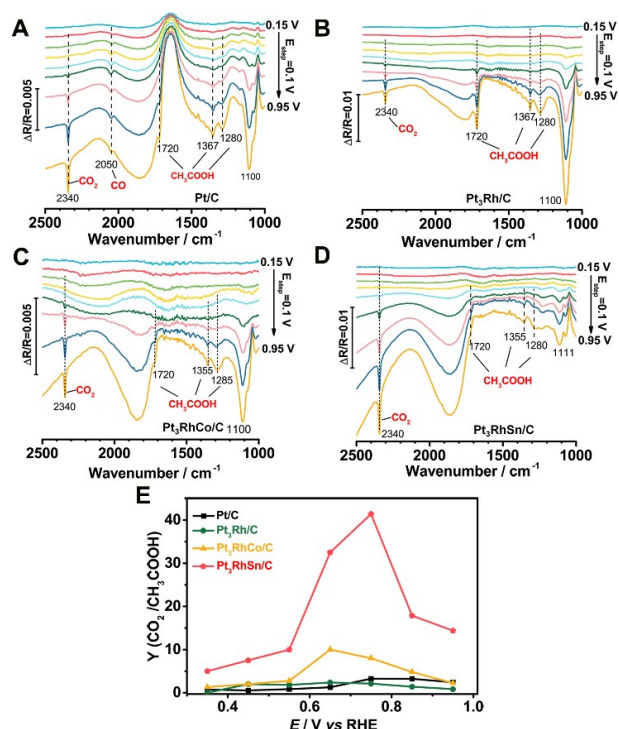


Figure 2. *In situ* FTIR spectra recorded during ethanol oxidation on (A) Pt/C, (B) $\text{Pt}_3\text{Rh/C}$, (C) $\text{Pt}_3\text{RhCo/C}$ and (D) $\text{Pt}_3\text{RhSn/C}$ by continuous stepped potentials from 0.15 V to 0.95 V in a mixture of 0.5 M $\text{CH}_3\text{CH}_2\text{OH}$ / 0.1 M HClO_4 , the step of the potential applied is 0.1 V. (E) Ratio of band intensities of $\text{CO}_2/\text{CH}_3\text{COOH}$ ($\sim 2343 \text{ cm}^{-1}/\sim 1280 \text{ cm}^{-1}$) on Pt/C, $\text{Pt}_3\text{Rh/C}$, $\text{Pt}_3\text{RhCo/C}$ and $\text{Pt}_3\text{RhSn/C}$ catalysts as a function of potentials. The signal intensity below 0.15 V is too weak, the potential range of E is set to 0.35 \sim 0.95 V for accuracy.

Discovered selectivity descriptor

DFT calculations of ethanol dehydrogenation and oxidation over Pt-Rh-M catalysts, were performed to identify the roles of Pt, Rh, and M, and the energy differences for key elementary steps of the complete oxidative path and intermediate adsorption. The reaction pathways, the most stable adsorption configurations of possible intermediates and energy profiles of ethanol oxidation on Pt (111) were firstly calculated to help modelling the bi-metallic or tri-metallic systems (Figure S9). The corresponding reaction energies, barriers and intermediate stabilities for C-H, O-H and C-C bonds cleavage

are listed in Table S7-S8. The cleavage of C-O bond to form C_2 hydrocarbons and some other unfavourable steps on Pt (111) surface were not taken into consideration in our computations.⁴³ Our calculation results about ethanol oxidation on Pt (111) are consistent with the previous reports,⁴⁴ indicating that C-C bond cracking takes more easily on the stable CH_2CO^* or CHCO^* intermediates. Then the CH^* and CO^* species are oxidized to CO_2 with the surface reactive oxygen species. (Figure S9 and Table S7). Thus, a higher C1 selectivity requires deeper dehydrogenation of ethanol. It starts from breaking $\text{C}_\alpha\text{-H}$ and O-H bonds, then forms stable adsorbed CH_3CO^* .⁴⁵ The by-products in EOR, mainly aldehyde and acetic acid, are derived from C_α -dehydrogenation of ethanol with low barrier. The C_β -dehydrogenation of CH_3CO^* on pure Pt surface with a high barrier (1.06 eV), is the rate-determining step (RDS). The side reaction ($\text{CH}_3\text{CO}^* + \text{H}_2\text{O}^* \rightarrow \text{CH}_3\text{COOH}^* + \text{H}^*$, $E_a = 0.73 \text{ eV}$) includes two elementary steps, $\text{H}_2\text{O}^* \rightarrow \text{H}^* + \text{OH}^*$ ($E_a = 0.73 \text{ eV}$) and $\text{CH}_3\text{CO}^* + \text{OH}^* \rightarrow \text{CH}_3\text{COOH}^*$ ($E_a = 0.56 \text{ eV}$) on Pt (111) surface. The reaction of OH^* and CH_3CO^* is more facile than the water dissociation. Thus, the difficulty of the side reaction to produce acetic acid is dependent on the water dissociation barrier. As shown in Figure 3A, the competition of CH_3CO^* dehydrogenation and water dissociation controls the selectivity to produce acetic acid. Once CH_2CO^* appears, the C-C bond cleavage to further C1 products become more facile. Hence, it is rational to set the difference of the water dissociation barrier ($E_{a,\text{H}_2\text{O}}$) and the C_β -dehydrogenation barrier ($E_{a,\text{CH}_3\text{CO}}$) as the selectivity descriptor on Pt-based catalysts.⁴⁶

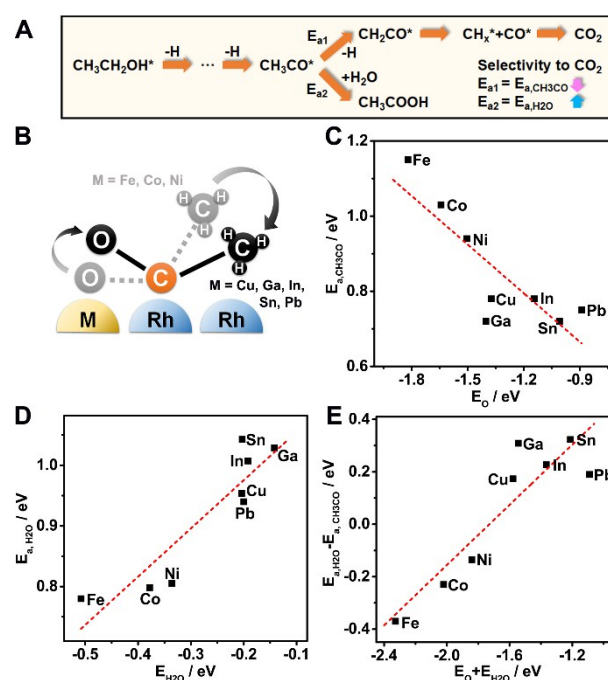


Figure 3. (A) Schematic ethanol dehydrogenation and oxidation steps towards the main product (CO_2) and the by-product (CH_3COOH). (B) Stable adsorption configurations of CH_3CO^* on Rh-Rh-M/Pt (111) sites. (C) Plot of the barriers of CH_3CO^* dehydrogenations on Pt-Rh-M (111) surfaces ($E_{a,\text{CH}_3\text{CO}}$) against the oxygen binding energy (E_O). (D) Plot of the barrier of water dissociation on Pt-Rh-M (111) surfaces ($E_{a,\text{H}_2\text{O}}$)

against the water binding energy ($E_{\text{H}_2\text{O}}$). (E) Plot of the sum of the oxygen and water binding energies ($E_{\text{O}}+E_{\text{H}_2\text{O}}$) against the difference of water dissociation barrier and CH_3CO^* dehydrogenation barrier ($\Delta E_{\text{a}} = E_{\text{a,H}_2\text{O}} - E_{\text{a,CH}_3\text{CO}}$).

We further replace the Pt atoms with Rh and the third metal ($M = \text{Fe}, \text{Co}, \text{Ni}, \text{Cu}; \text{Ga}, \text{In}, \text{Sn}, \text{Pb}$) to investigate the roles of M in the ethanol dehydrogenation and oxidation steps, and how M controls the selectivity and activity of EOR. The atom ratios of Pt/Rh/ M on surface layers were approximately fixed at a ratio of 2:1:1 according to the XPS results in Table S9. To see the electronic effect of the third metal on the Pt and Rh, we constructed the 2×2 fcc-structured Pt_2RhM to cleave the Pt-Rh- M (111) surface. Firstly, we calculated the most stable configurations and dehydrogenation barriers of CH_3CO^* on possible adsorption sites with the C and O bound on different metal sites. The CH_3CO^* adsorbed on Rh-Rh- M /Pt (111) sites owns the lowest dehydrogenation barrier among possible site combinations. The 2×2 Pt_2RhM (111) surfaces do not have such a Rh-Rh- M site for stable CH_3CO^* adsorption, so we constructed a larger 3×3 Rh and M doped Pt (111) surfaces, with the surface Pt atoms replaced by the Rh and M atoms. Typical surfaces that can stabilize the CH_3CO^* with C_α , C_β and O bonded on different metal sites are shown in Figure S10. It is noted that the addition of Rh site lowers the barrier of C_β -H breakage of CH_3CO^* , especially on the Rh (C_β), Rh (C_α) and M (O) sites (Rh-Rh- M /Pt (111)), suggesting that more Rh sites on Pt-Rh- M surface may facilitate the splitting of C_β -H bond (Table S10). Thus, Rh-Rh- M /Pt (111) sites were used to further investigate the composition effect of M on the CH_3CO^* -dehydrogenation. As shown in Figure 3B, the chair-like adsorption configurations of CH_3CO^* with C_α anchored on the top site of Rh, display regular changes with the strength of O- M interaction. The weaker the O- M interaction, the closer the $-\text{CH}_3$ group gets to the surface for C_β -dehydrogenation. The distances of O- M and C_β -Rh as well as the $E_{\text{a,CH}_3\text{CO}}$ on Rh-Rh- M surface indicate that the addition of Sn, Ga, Pb, In and Cu favors the C_β -dehydrogenation steps more than that of Fe, Co and Ni due to weaker O- M interactions (Table S11). Crystal orbital overlap populations (COOP) were used to analyse the electron filling of O- M bond. Here we take Pt-Rh-Sn and Pt-Rh-Co surfaces (Rh-Rh- M adsorption sites) as typical examples (Figure S11). More antibonding orbitals below the Fermi level present in the Sn-O COOP than the Co-O COOP, indicating a weaker Sn-O interaction, even a repulsion in Sn-O, which reflects their intrinsic electronic structures of additive metals. Obviously, main group metals may be the better promoters for C_β -dehydrogenation step owing to their optimal O- M interactions and synergistic effect with Rh and Pt. These additive metals make different influences on the barrier of C_β -dehydrogenation. Considering the selectivity to CO_2 against CH_3COOH could be controlled by the difference of C_β -dehydrogenation and water dissociation barriers, we calculate the water dissociation barrier on Pt-Rh- M surfaces (Table S10). For Pt-Rh-Sn surface, the C_β -dehydrogenation barrier (0.72 eV) is lower than the water dissociation barrier (1.04 eV). However, for Pt-Rh-Co catalyst, the C_β -dehydrogenation barrier (1.03 eV) is higher than the water dissociation one

(0.80 eV). The Pt-Rh-Sn catalyst shows a greater selectivity towards CO_2 than Pt-Rh-Co catalyst, which agrees with the *in situ* FTIR results that the $\text{Pt}_3\text{RhSn}/\text{C}$ owns a higher $\text{CO}_2/\text{CH}_3\text{COOH}$ ratio than $\text{Pt}_3\text{RhCo}/\text{C}$. Therefore, ΔE_{a} ($E_{\text{a,H}_2\text{O}} - E_{\text{a,CH}_3\text{CO}}$) can be used as a selectivity descriptor to screen ideal active metal sites.

To get a more simple and straightforward descriptor, the scaling relation between oxygen binding energy (E_{O}) and $E_{\text{a,CH}_3\text{CO}}$ with a negative correlation was established ($E_{\text{a,CH}_3\text{CO}} = -0.43E_{\text{O}} + 0.28$, $R = 0.85$), as the O- M interactions were demonstrated to be the intrinsic dominator of the C_β -dehydrogenation (Figure 3C, Table S10 and S12). At the same time, there also exists a scaling relation between H_2O binding energy ($E_{\text{H}_2\text{O}}$) and $E_{\text{a,H}_2\text{O}}$ with a positive correlation on Pt-Rh- M surface ($E_{\text{a,H}_2\text{O}} = 0.78E_{\text{H}_2\text{O}} + 1.13$, $R = 0.91$), as water dissociation is an endothermic reaction (Figure 3D, Table S12-13). From the above, a more straightforward and convenient correlator of EOR selectivity, $0.78E_{\text{H}_2\text{O}} + 0.43E_{\text{O}} + 0.85$, was discovered on the Pt-Rh- M surface, generated from ΔE_{a} . We further simplified the descriptor as $E_{\text{O}}+E_{\text{H}_2\text{O}}$ for a larger application on Pt-based surfaces for EOR, as there exists a linear relation between $E_{\text{H}_2\text{O}}$ and E_{O} ($E_{\text{H}_2\text{O}} = 0.31E_{\text{O}} + 0.15$, $R = 0.78$).⁴⁷ A more positive value of $E_{\text{O}}+E_{\text{H}_2\text{O}}$, corresponding to a higher ΔE_{a} , represents a higher EOR selectivity to CO_2 , which matches well with the experimental results (Figure 3E). Pt-Rh-Sn with a higher $E_{\text{O}}+E_{\text{H}_2\text{O}}$ displayed higher CO_2 selectivity than Pt-Rh-Co. A weaker O-Sn interaction lowers more the $E_{\text{a,CH}_3\text{CO}}$ on Pt-Rh-Sn than Pt-Rh-Co. Besides, a stronger binding strength of H_2O on Pt-Rh-Co makes water dissociation easier on Pt-Rh-Co than Pt-Rh-Sn. The simplified descriptor $E_{\text{O}}+E_{\text{H}_2\text{O}}$ might be helpful to a large scale screening of the selectivity in Pt-based EOR catalysts, though its physical basis is not as clear as the descriptor of ΔE_{a} . The descriptor of ΔE_{a} not only explained the intrinsic reasons why $\text{Pt}_3\text{RhM}/\text{C}$ catalysts showed different CO_2 selectivity in *in situ* FTIR, but also predicted a trend in EOR selectivity of Pt-based EOR catalysts. Although Ga and Pb display a little deviation from the linear relationship, it is still instructive to screen the EOR catalysts with high selectivity.

Discovered activity descriptor

A key factor that controls the activity is the binding strength of surface stable adsorbates in thermodynamics (Figure 4A).⁴⁸ Timely removing of strong bound species, such as CO, would bare more active sites for higher activity and durability. The formation energies (E_{form}) of adsorbates with respect to gas-phase ethanol on Pt (111) were listed to compare the relative adsorption stability of all reaction intermediates in ethanol decomposition (Table S8).⁴⁴ The C1 products exhibit strong adsorption on Pt (111) surface compared with other intermediates, which agrees with the general view that Pt is easily poisoned by CO and other CH_x species.

To investigate the effect of intrinsic electronic structures of Pt-Rh- M surfaces on the adsorption of intermediates, we calculated the d-band centres of Pt and Rh on Pt_2RhM (Figure 4B and Table S14). The addition of main group metals shifts down the d-band centres of Pt and Rh more than transition metals do, leading to a weaker adsorption of C1 species on Pt-

Rh-M (M = Ga, In, Sn, Pb) surface. The positions of d-band centre on transition metal doped Pt-Rh-M are different from that on main group metal doped Pt-Rh-M. The less filled d-band of Fe, Co, Ni and Cu causes the antibonding σ band more above the Fermi level, resulting in a smaller Pauli repulsion of surface atoms to CO. Thus the CO bond strength increases with the higher d-band centre (Figure 4C).⁴⁹ Although CO is bonded to the top site of Rh with similar adsorption energies on all Pt₂RhM surfaces, the CO adsorption on the hollow site of Pt-Rh-M are more susceptible to the electronic effect of M. Here we put the CO adsorption on *fcc*-phased pure M (111) surface for comparison (Table S15). CO seems more difficult to be adsorbed on the main group metal surfaces than the transition metal ones. As a proof, we use CO stripping to evaluate the performance of CO oxidation on Pt-Rh-M surface by means of experiments.⁴⁰ Generally, the lower the onset potential of CO oxidation, the higher the CO tolerance. As shown in Figure S12, the onset potentials show similar trends that CO oxidation takes more easily on Pt₃RhM/C (Ga, In, Sn, Pb) surfaces. Hence, main group metals (Ga, In, Sn, Pb) outperform transition metals (Fe, Co, Ni, Cu,) in the enhancement of CO tolerance.

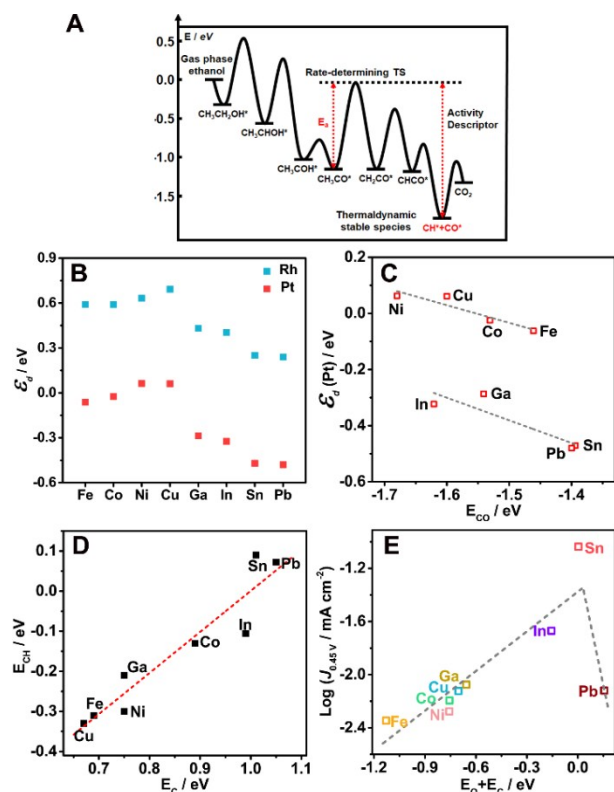


Figure 4. (A) Schematic potential energy surface of ethanol on Pt (111). The rate-determining transition state (TS) is considered to be the CH₃CO dehydrogenation one with a highest activation energy. And the most stable species are considered to be the CH and CO adsorbates. (B) d-band centres (ϵ_d) of Pt and Rh on Pt-Rh-M surface. (C) Plot of the Pt d-band centre against E_{CO} . (D) Plot of the binding energy of CH (E_{CH}) on Pt-Rh-M (111) surfaces against the carbon binding energy (E_C). (E) Plot of the sum of the oxygen and carbon

binding energies (E_O+E_C) against the logarithm of current density at 0.45 V. DOI: 10.1039/C8TA03320J

The EOR activity can be affected by both the apparent activation energy and the adsorption energy of the most stable C1 species.⁴⁵ As shown in Figure 4A, although the CH₃CH₂OH-dehydrogenation at the first step goes through the highest energy of transition state (TS) in the potential energy surface, the barrier is still lower than E_{a,CH_3CO} (Table S10). And CH₃CO* is a thermodynamically favored intermediate. From this point of view, the RDS can be considered as the CH₃CO*-dehydrogenation, and it is rational to conclude that the apparent activation energy depends on E_{a,CH_3CO} . Based on the scaling relation of E_{a,CH_3CO} and E_O , E_O would be a good correlator of the apparent activation energy on the Pt-Rh-M surfaces. Furthermore, a scaling relations between the adsorption energies of CH and E_C with a positive correlation were found ($E_{CH} = 0.96E_C + 0.97$, $R = 0.93$), the adsorption energy of C1 species can be described by the binding energy of carbon atom (E_C) (Figure 4D, Table S12-S13).⁵⁰ There also exist scaling relations between the adsorption energies of CO, CH and H (Figure S13). The regulation of E_C and CO stripping results suggest that main group metals (Ga, In, Sn, Pb) outperform transition metals (Fe, Co, Ni, Cu,) in the enhancement of C1 species tolerance. A higher activity requires both lower E_{a,CH_3CO} (more positive E_O) and a weaker C1 adsorption (more positive E_C).⁴⁵ Similarly, we set the E_O+E_C as a simplified activity descriptor which is generated from the energy difference of the rate-determining TS and the thermal dynamic species (Figure 4A). According to the Arrhenius type law ($j \propto e^{-E_{ads}/RT}$), there exists a linear relationship between the logarithm of current density and the adsorption energies of stable intermediates. As indicated in Figure 4E, a great volcano relationship between the descriptor (E_O+E_C) and EOR activity ($\log j$) at 0.45 V based on theoretical and experimental results was established. The as-synthesized Pt₃RhPb/C did not show improved performance with a higher calculated E_O+E_C value (0.16 eV) on Pt-Rh-Pb surface than Pt₃RhSn/C. The too weak adsorptions of C and O on Pb make it hard for the further oxidation of C1 species. At the same time, Pt-Rh-Co surface with a lower E_O+E_C value (-0.73 eV) displayed limited enhancement of EOR activity, as indicated in LSV tests. From this point, the EOR activity can be improved by constructing a proper surface with a not too strong and not too weak interaction with surface stable adsorbates. The distinguishable E_O+E_C value from -1.13 eV to 0.16 eV between transition metal doped and main group metal doped catalysts makes it valid to identify EOR catalysts with high activity. Here the addition of Ni, Co, Cu and Ga exhibits similar E_O+E_C values, corresponding to their small difference in activity. The discovery of E_O+E_C is closely related to the adsorption configurations of intermediates, where C and O atoms of most intermediates are bonded to the surface. Among these Pt-Rh-M surfaces, Pt-Rh-Sn exhibits an optimum E_O+E_C value (0 eV). The combination of E_O and E_C as descriptor can be seen as the replacement of the two-dimensional plotting separately. This

reveals an overall effect of rate-determining steps and surface strong bonded species.

It is worth mentioning that the surface atomic order of the constructed Pt-Rh-M models hardly affects these regulations on a large scale. A simplified model that both the surface and the sublayer atoms of Pt (111) were replaced by Rh and M, was constructed and then computed as a reference to see the generality of our model. We used several different Pt-Rh-M models to see the C, H, O and small molecules adsorptions. There exist the same trends in the binding strength of the adsorbates on Rh, M doped Pt (111) surfaces as the Pt₂RhM (111) surfaces (Table S16). Thus, these similar trends imply the significant contribution of the electronic effect caused by the addition of M atoms, which were also observed on the pure fcc-phased metal close-packed surfaces (Table S15). These monometallic models were used to investigate the electronic effect of monometallic surfaces on the adsorption of small molecules as comparisons to those Pt₂RhM models. Rh with a fairly strong binding of C and O atoms, obviously needs to be alloyed with M to prevent site blocking. While transition metals could not help to improve the site blocking of stable adsorbed intermediates on Rh surface. The addition of Sn markedly optimizes C-M interaction and O-M interaction, and the catalytic rate has a volcano-shaped correlation to the descriptor with a maximum at the optimum value of $E_{\text{O}} + E_{\text{C}}$.⁵¹

The DFT calculations indicate that the addition of main group metal increases the difference of the barrier of water dissociation and C_β-dehydrogenation on a larger scale than that of transition metals, resulting in high EOR selectivity. Then the additive metals further modify the electronic structures of Pt-Rh-M surface to regulate the adsorption strength of strong bonding intermediates. The main group metal doped Pt-Rh surfaces not only possess lower apparent activation energy, but also exhibit better tolerance against C1 species than transition metal doped ones, both of which contribute to the enhanced EOR activity. As there exist a series of scaling relations between the barriers of key elementary steps and the binding energies of some small molecules, the selectivity and activity descriptors are simplified into $E_{\text{O}} + E_{\text{H}_2\text{O}}$ and $E_{\text{O}} + E_{\text{C}}$. The discovered descriptors elucidate the intrinsic dominant factors of EOR performance, and provide a general trend of active and selective multicomponent platinum nanoalloys towards EOR.

Considering the superior EOR performance of Pt₃RhSn/C catalyst, extended X-ray absorption fine structure (EXAFS) analysis was carried out to identify the local coordination structure of Pt (Figure S14 and Table S17-S18). The CNs of Pt-Pt, Pt-Rh and Pt-Sn suggest the formation of Pt-Rh-Sn alloy and bulk enrichment of Pt. The PXRD pattern of Pt₃RhSn/C catalyst was further quantitatively analysed by Rietveld refinement (Figure S15-16 and Table S19), indicating a weight ratio of 84:16 for fcc-structured Pt₃Sn and Pt₃Rh₆Sn. According to the electrochemical results (Pt₃RhSn/C > Pt₃Sn/C > Pt₃Rh/C > Pt/C in Figure 1C), both fcc-like Pt₃Sn (rich) and fcc-like Pt₃Rh₆Sn domains are active components.⁵²⁻⁵⁵ The decisive factors for high EOR performance of as-synthesized Pt₃RhSn/C can be reasonably interpreted. In experiments, we realized controlled synthesis of Pt₃RhM/C without any surfactant, which

prevented the active sites from being covered by organic molecules. Deliberate H₂ treatment at 600 °C induces more Rh to expose on the surface (Table S20), which not only accelerates the C_β-dehydrogenation but also makes the surface of Pt₃RhM/C consistent with the calculated Rh-Rh-M surface, and thus results in the greatly increased activity (Figure S17). No pronounced change of the valence of Pt, Rh and Sn was found before and after catalytic tests, proving the electrochemical stability of Pt₃RhSn/C nanocatalyst (Figure S18 and Table S21). However, the other additive metals (M) are easily oxidized in air and electrochemical reactions accelerated the oxidation of M (Table S22). From the point of theoretical calculations, the weakest Sn-O interaction benefits CH₃CO-dehydrogenation to make splitting C-C bond easier. While relatively high water dissociation barrier of Pt-Rh-Sn surface suppresses the formation of acetic acid. Furthermore, Pt-Rh-Sn surface optimize the adsorption of C1 species, which combines with the lowest apparent activation energy for the highest activity and durability. From an overall perspective, the tailored electronic structures of Pt-Rh-M by introducing different additive earth-abundant metals make greater impacts than the geometric effect on their EOR performances. Thus, the phase segregation of as-synthesized Pt₃RhPb/C hardly affects the overall trends in selectivity and activity. Here the applied potential and the solvation pH values were not included in the computations, as the dehydrogenation steps are all single electron transfer ones, with approximately the same change of the potential and solvation dependent barriers. The distinguishable $E_{\text{O}} + E_{\text{H}_2\text{O}}$ and $E_{\text{O}} + E_{\text{C}}$ of Pt-Rh-M surfaces exactly reflect the intrinsic doping effect both electronically and catalytically at the atomic scale. At the same time, the intermediates of alcohols (methanol, ethanol, glycols, etc.) oxidation reactions are basically binding to the surface metal atoms with the directly O-M and C-M bonds.⁵⁶⁻⁵⁹ The tradeoff of binding strength of surface oxygen and carbon species can also be exploited as the descriptor for AORs. For C₂+ AORs with more elementary steps, more intermediates with different adsorption strength should be considered to screen highly active surface. In the view of the mechanism research of AOR, EOR is the most typical model reaction. The research strategies and discovered catalytic descriptors would make great significances on the design and synthesis of highly efficient catalysts for methanol and C₂+ AORs.

Conclusions

A set of Pt₃RhM nanoalloys (M= Fe, Co, Ni, Cu; Ga, In, Sn, Pb) supported on carbon with a similar geometric structure and crystallize size, were controllably synthesized by one-pot solvothermal method. Electrochemical measurements and *in situ* FTIR indicate that main group metals contribute more to the improved EOR activity and selectivity at low potential. Especially, the specific activity of Pt₃RhSn/C nanocatalyst are 67 times higher than that of commercial Pt/C catalyst at 0.45 V. DFT calculations demonstrate the effective descriptors of EOR selectivity and activity: $E_{\text{O}} + E_{\text{H}_2\text{O}}$ and $E_{\text{O}} + E_{\text{C}}$, respectively. For Pt-Rh-M surface, the roles of Rh and M active sites have

been defined: (1) Rh and M control the adsorption configurations of key intermediates and thus change the barrier of RDS; (2) The additive M further influences the adsorption and dissociation energies of water, which determine the difficulty to produce acetic acid; (3) M also tunes the adsorption strength of stable intermediates by shifting the d-band centres of Pt and Rh, and thus modulate the reaction activity. The addition of IIIA and IVA metals (Ga, In, Sn, Pb) increases more $E_{a,H_2O}-E_{a,CH_3CO}$ value than that of late 3d transition metals (Fe, Co, Ni, Cu) for higher CO_2 selectivity. In addition, the main group metal alloyed Pt-Rh surface with the tailored electronic structure displays better catalytic performance. A volcano-shaped relationship between the EOR activity of Pt_3RhM/C catalysts and E_O+E_C of Pt-Rh-M surface, which exactly reflects the intrinsic composition and electronic effects on EOR.

Combining experimental framework with theoretical modelling, a series of scaling relations between surface composition and intermediates are uncovered to understand these catalytic trends. The discovered descriptors as a basis, not only could clarify key limitations among known catalysts systems but also provided new insights into successful strategies to develop improved electrocatalysts for AORs.

Experimental

Chemicals

Platinum(II) 2,4-pentanedionate ($Pt(acac)_2$, Pt wt. % >48.0%, Alfa Aesar Chemicals Co. Ltd, China), $RhCl_3 \cdot 3H_2O$ (A.R., Sinopharm Chemical Reagent Co. Ltd, China), N, N-dimethylformamide (DMF, A.R., Xilong Chemical Co. Ltd, China), Benzoic acid (C_6H_5COOH , AR, Xilong Chemical Co. Ltd, China), Iron(III) acetylacetonate ($Fe(acac)_3$, 98%, Shanghai Ourchem Co. Ltd, China), Nickel(II) acetylacetonate ($Ni(acac)_2$, 96%, J&K), Cobalt(II) 2,4-pentanedionate ($Co(acac)_2$, Alfa Aesar), Copper(II) acetylacetonate ($Cu(acac)_2$, 97%, Sigma-Aldrich), Gallium(III) nitrate hydrate ($Ga(NO_3)_3 \cdot xH_2O$, 99.9%, Alfa Aesar), Indium(III) 2,4-pentanedionate ($In(acac)_3$, 98%, Alfa Aesar), Tin(IV) bis(acetylacetonate) dichloride ($Sn(acac)_2Cl_2$, 98%), Lead(II) acetate trihydrate ($Pb(OAc)_2 \cdot 3H_2O$, 99%), Xilong Chemical Co. Ltd, China), carbon black (Vulcan XC-72), ethanol (A.R.), Pt/C catalyst (20 wt% Pt, Shanghai Hesent Electric Co. Ltd, China), acetone (A.R.), cyclohexane (A.R.), deionized water (Millipore, 18.2 $M\Omega \cdot cm$).

Synthesis of Pt_3RhM/C

0.03 mmol of $Pt(acac)_2$, 0.01 mmol of $RhCl_3$ and 0.01 mmol of $M(acac)_x$ (except $Ga(NO_3)_3 \cdot xH_2O$), 3 mmol of C_6H_5COOH and 32 mg of commercial carbon black (Vulcan XC72R carbon) dispersed in 10 mL of DMF were added into a 25 mL vial. After 16 h reaction at 160 °C in an oil bath, the resulting products were collected by centrifugation and washed with an ethanol/acetone mixture. The precipitate was dried for 12 h at 70 °C, followed by post-treatment at 600 °C for 1 h in H_2/Ar atmosphere. The synthesis of Pt_3RhSn_x/C ($x=0.5, 1.5$) is the same as that of Pt_3RhSn/C except adding 0.005 mmol or 0.02

mmol of $Sn(acac)_2Cl_2$. The synthesis of Pt_3Sn/C is the same as that of Pt_3RhSn/C without adding $RhCl_3$. DOI: 10.1039/C8TA03320J

Structural characterization

Transmission electron microscope (TEM), high-resolution transmission electron microscope (HRTEM), energy dispersive X-ray spectroscopy (EDS), and high-angle annular dark-field scanning transmission electron microscopy (HAADF-STEM) EDS line and mapping scan analyses were conducted on a FEG-TEM (JEM-2100F, JEOL, Japan) operated at 200 kV. Powder X-ray diffraction (PXRD) analysis was performed on a Rigaku D/MAX-2000 diffractometer (Japan). Inductively coupled plasma atomic emission spectroscopy (ICP-AES) analysis was conducted on a Profile Spec ICP-AES spectrometer (Leeman, U.S.A.). X-ray photoelectron spectroscopy (XPS) analysis was taken on an Axi Ultra imaging photoelectron spectrometer (Kratos, UK). Pt L3-edge extended X-ray absorption fine structure (EXAFS) analysis was carried out on the BL14W1 beamline of Shanghai Synchrotron Radiation Facility (SSRF) operated at 3.5 GeV under "top-up" mode with current of 240 mA. Pt foil was used as reference samples. The spectra of reference sample were collected in transmission mode, the spectra of Pt_3RhSn/C were collected in fluorescence mode. All of the collected spectra were processed and analysed using Athena and Artemis code within the IFEFFIT package.

Electrochemical Measurements

Electrochemical measurements were conducted on a CHI 760E electrochemical analyzer (CH Instrument, TX, U.S.A.) in a standard three electrode cell. In the three-electrode system, a glassy carbon (5 mm in diameter) electrode was used as the working electrode; a platinum foil was used as the counter electrode; a KCl-saturated Ag/AgCl electrode was used as the reference electrode. 20 μL of the colloid NPs solution was dropped on a glassy carbon electrode and dried for preparing the working electrode. Then, the samples on the working electrode were covered by 10 μL of 0.2 wt % Nafion (Sigma-Aldrich) solution and dried for further electrochemical measurements. All the measurements were performed at room temperature, and the electrolyte used was freshly made. The electrochemically active surface area (ECSA) of each sample was calculated from the H adsorption area in the cathodic scan of CV measurement, which was carried out in 0.1 $mol \cdot L^{-1}$ $HClO_4$ aqueous solution at a sweep rate of 20 $mV \cdot s^{-1}$. The calculation equation of ECSA is $ECSA (cm^2) = Q_H / 210 \mu C \cdot cm^{-2}$. The EOR property of each sample was evaluated by its quasi steady polarization curve, which was obtained by linear sweep voltammetry in N_2 -saturated 0.5 $mol \cdot L^{-1}$ $CH_3CH_2OH/0.1 mol \cdot L^{-1} HClO_4$ aqueous solution at a sweep rate of 1 $mV \cdot s^{-1}$. Before the evaluations of trimetallic nanocatalysts toward EOR, a hundred cycles of cyclic voltammetry ranged from 0.056 to 1.456 V at a sweep rate of 50 $mV \cdot s^{-1}$ were applied to remove the residues on surfaces. All the potentials used were normalized by reversible hydrogen electrode (RHE). The reference electrode has been calibrated by RHE.

The CO stripping tests were conducted in 0.1 M $HClO_4$ electrolyte. The working electrode was lowered into N_2 -

saturated electrolyte at 0.06 V for 15 min. Then, the gas is switched to the CO and the bubbling occurs for further 15 min, followed by gas switched to N₂ (30 min) in order to remove the CO from electrolyte. The whole procedure occurs under potential control at 0.06 V. Two CV were performed between 0.06 ~ 1.0 V with 50 mV s⁻¹. No electrochemical CO oxidation was observed in the second CV, indicating the full conversion of adsorbed CO.⁴⁰

In Situ Fourier transform infrared Spectroscopy (FTIRS)

A Nicolet Nexus 870 Fourier transform infrared spectrometer equipped with a mercury cadmium telluride detector cooled with liquid nitrogen was employed in the in situ FTIRS electrochemical study. A calcium fluoride window and an in situ EC-IR thin-layer cell were applied in the test. The reference spectrum was collected at 0.05 V vs RHE in 0.5 M CH₃CH₂OH/0.1 M HClO₄. Spectra under a continuous stepped potential from 0.15 V ~ 0.95 V with 200 scan and 8 cm⁻¹ resolution were acquired. To subtract the signals from background, the spectrum at each potential was normalized by the reference spectrum as follows:

$$\frac{\Delta R}{R}(E_s) = \frac{R(E_s^i) - R(E_R)}{R(E_R)}$$

$R(E_R)$ and $R(E_s^i)$ were the spectrum at reference potential and tested potential, respectively.

Computational methodology

All calculations were performed using the Vienna Ab-initio Simulation Package (VASP)⁶⁰⁻⁶² with the exchange-correlation energy functional of Perdew-Burke-Ernzerhof generalized gradient approximation (GGA-PBE).⁶³ The core electron interactions were described using projector augmented-wave (PAW) pseudopotentials.⁶⁴ The kinetics cut-off energy for the plane-wave basis was set to 400 eV.

The ethanol dehydrogenation reactions were carried out on Pt (111) surface with 3 × 3 unit cell with six layers. The top three layers were relaxed during the optimization process, and the bottom three layers were fixed. The vacuum region was around 15 Å between the slabs. The 5 × 5 × 1 Monkhorst-Pack k-point sampling was automatically generated in the Brillouin zone. The K-points and cut-off energy were tested to be met with errors less than 1 meV/atom. Each structure was relaxed until the residual force was less than 0.05 eV/Å. All the transition states were characterized via Climbing-Image Nudged Elastic Band (CI-NEB) method with Limited-memory Broyden-Fletcher-Goldfarb-Shanno (LBFGS) algorithm.^{65, 66} The transition states were identified by vibrational analysis and only one imaginary eigenvalue was acquired. The vibration calculations were also performed to validate the zero-point energy (ZPE) correlation. Spin polarization was included in the calculation of Fe, Co, Ni.

For EOR dehydrogenation and small molecules adsorbed on Pt-Rh-M (M=Fe, Co, Ni, Cu, Ga, In, Sn, Pb.) surfaces, the uniformed Pt₂RhM fcc structures were constructed to mimic the XPS results due to the surface ratio of Pt:Rh:M approximate to 2:1:1. All 2 × 2 Pt₂RhM (111) surfaces with 4-

layer slabs were cleaved with 15 Å vacuum region. 4 × 4 Pt₂RhM (111) surfaces with 1/16 monolayer adsorptions were also computed to be compared with the 2 × 2 surface, and the same adsorption tendency was obtained.

To see the rationality of the surface model and the dominant factor of the electronic effect, we further construct other surface structures as comparison models. The 3 × 3 PtRhM/Pt (111) surfaces are simulated by replacing the Pt atoms by Rh and M atoms on the surface and sub-surfaces. These surfaces were modelled by four-layer slabs with the top three layers relaxed and the bottom one fixed.

The binding energies of C, H, O and small molecule are defined as: $E_{\text{bind}} = E_{\text{ads/surface}} - E_{\text{surface}} - E_{\text{adsorbate}}$, where $E_{\text{ads/surface}}$ is the total energy of the adsorbate on the metal, and $E_{\text{adsorbate}}$ is with respect to the gas phase H₂, H₂O or solid phase diamond carbon.

The reaction energy (ΔE) of reactions and the reaction barrier (E_a) was calculated by $\Delta E = E_{\text{FS}} - E_{\text{IS}}$ and $E_a = E_{\text{TS}} - E_{\text{IS}}$, where E_{FS} represents the total energies of all products adsorbed separately on metal surfaces. E_{TS} and E_{IS} are the energies of the transition states and initial states. The d-band centers were derived by $\epsilon_d = \int \rho(E) E dE / \int \rho(E) dE$, where $\rho(E)$ represents the electronic density of the state distribution. Here the number of bands was set to 192 with a large number of empty bands in the calculation, so that all occupied bands were taken into computation. The projected COOP curves were analysed and obtained using lobster-2.1.0 package.⁶⁷ The DFT values of the lattice parameters were only 1.5% larger than the experimental values (Table S12 and S1), so the DFT computations were reasonable and accurate enough.

Conflicts of interest

There are no conflicts to declare.

Acknowledgements

This work was supported by the National Natural Science Foundation of China (No. 21771009, 21573005, and 21621061), the National Key Research and Development Program of MOST of China (No. 2016YFB0701100), and the Beijing Natural Science Foundation. The computational work is supported by High-performance Computing Platform of Peking University.

Author contributions

Y.-W.Z. conceived this research project. L.-X.D., X.-Y.W. and Y.-W.Z. designed this study. L.-X. D., S.-S.Y. collected the experimental data. X.-Y.W., P.-J.R. and X.-D.W. collected the theoretical data. T.Z. contributed the TEM characterizations. B.N. and R.S. did the analyses of EXAFS data. J.-Y.Y. and Z.-Y.Z. conducted the in situ FTIR experiments. L.-X.D., X.-Y.W. and Y.-W.Z. wrote the paper. C.-H.Y. discussed the results and refined the ideas. All authors commented this manuscript.

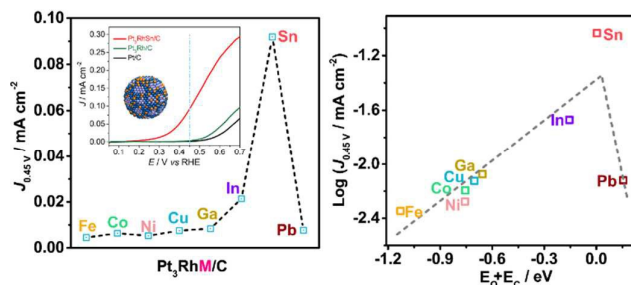
References

- 1 A. K. Agarwal, *Prog. Energ. Combust.* 2007, **33**, 233–271.
- 2 J. Hill, E. Nelson, D. Tilman, S. Polasky and D. Tiffany, *PNAS*, 2006, **103**, 11206–11210.
- 3 M. Z. F. Kamarudin, S. K. Kamarudin, M. S. Masdar and W. R. W. Daud, 2013, **38**, 9438–9453.
- 4 C. Lamy, A. Lima, V. LeRhun, F. Delime, C. Coutanceau and J. M. Léger, *J. Power Sources* 2002, **105**, 283–296.
- 5 E. Antolini, *J. Power Sources* 2007, **170**, 1–12.
- 6 R. B. Kutz, B. Braunschweig, P. Mukherjee, R. L. Behrens, D. D. Dlott and A. Wieckowski, *J. Catal.* 2011, **278**, 181–188.
- 7 B. W. Zhang, T. Sheng, Y. X. Wang, X. M. Qu, J. M. Zhang, Z. C. Zhang, H. G. Liao, F. C. Zhu, S. X. Dou, Y. X. Jiang and S. G. Sun, *ACS Catal.* 2017, **7**, 892–895.
- 8 F. Saleem, Z. C. Zhang, B. Xu, X. B. Xu, P. L. He and X. Wang, *J. Am. Chem. Soc.* 2013, **135**, 18304–18307.
- 9 W. Zhu, J. Ke, S. B. Wang, J. Ren, H. H. Wang, Z. Y. Zhou, R. Si, Y. W. Zhang and C. H. Yan, *ACS Catal.* 2015, **5**, 1995–2008.
- 10 K. Jiang, L. Bu, P. Wang, S. J. Guo and X. Q. Huang, *ACS Appl. Mater. Inter.* 2015, **7**, 15061–15067.
- 11 A. Kowal, M. Li, M. Shao, K. Sasaki, M. B. Vukmircovic, J. Zhang, N. S. Marinkovic, P. Liu, A. I. Frenkel and R. R. Adzic, *Nat. Mater.* 2009, **8**, 325–330.
- 12 N. Erini, R. Loukrakpam, V. Petkov, E. A. Baranova, R. Yang, D. Teschner, Y. Huang, S. R. Brankovic and P. Strasser, *ACS Catal.* 2014, **4**, 1859–1867.
- 13 N. Erini, P. Krause, M. Gliech, R. Yang, Y. Huang and P. Strasser, *J. Power Sources* 2015, **294**, 299–304.
- 14 N. Erini, S. Rudi, V. Beermann, P. Krause, R. Yang, Y. Huang and P. Strasser, *ChemElectroChem* 2015, **2**, 903–908.
- 15 C. Hu, H. Cheng, Y. Zhao, Y. Hu, Y. Liu, L. Dai and L. Qu, *Adv. Mater.* 2012, **24**, 5493–5498.
- 16 E. Méndez, J. L. Rodríguez, M. C. Arévalo and E. Pastor, *Langmuir* 2002, **18**, 763–772.
- 17 M. Li, D. A. Cullen, K. Sasaki, N. S. Marinkovic, K. More and R. R. Adzic, *J. Am. Chem. Soc.* 2013, **135**, 132–141.
- 18 L. Jiang, G. Sun, S. Sun, J. Liu, S. Tang, H. Li, B. Zhou and Q. Xin, *Electrochim. Acta* 2005, **50**, 5384–5389.
- 19 M. Li, W. P. Zhou, N. S. Marinkovic, K. Sasaki and R. R. Adzic, *Electrochim. Acta* 2013, **104**, 454–461.
- 20 J. K. Nørskov, T. Bligaard, J. Rossmeisl, C. H. Christensen, *Nat. Chem.* 2009, **1**, 37–46.
- 21 E. Skúlason, V. Tripkovic, M. E. Björketun, S. Gudmundsdóttir, G. Karlberg, J. Rossmeisl, T. Bligaard, H. Jónsson and J. K. Nørskov, *J. Phys. Chem. C* 2010, **114**, 18182–18197.
- 22 J. K. Nørskov, J. Rossmeisl, A. Logadottir and L. Lindqvist, *J. Phys. Chem. B* 2004, **108**, 17886–17892.
- 23 S. J. Hwang, S. K. Kim, J. G. Lee, S. C. Lee, J. H. Jang, P. Kim, T. H. Lim, Y. E. Sung and S. J. Yoo, *J. Am. Chem. Soc.* 2012, **134**, 19508–19511.
- 24 P. Ferrin and M. Mavrikakis, *J. Am. Chem. Soc.* 2009, **131**, 14381–14389.
- 25 J. Rossmeisl, P. Ferrin, G. A. Tritsarlis, A. U. Nilekar, S. Koh, S. E. Bae, S. R. Brankovic, P. Strasser and M. Mavrikakis, *Energy Environ. Sci.* 2012, **5**, 8335–8342.
- 26 A. C. Lausche, J. S. Hummelshøj, F. Abild-Pedersen, F. Studt, J. K. Nørskov, *J. Catal.* 2012, **291**, 133–137.
- 27 W. An, Y. Men, J. Wang, and P. Liu, *J. Phys. Chem. C* 2017, **121**, 5603–5611.
- 28 P. Ferrin, D. Simonetti, S. Kandoi, E. Kunkes, J. A. Dumesic, J. K. Nørskov and M. Mavrikakis, *J. Am. Chem. Soc.* 2009, **131**, 5809–5815.
- 29 J. Zaffran, C. Michel, F. Delbecq, and P. Sautet, *J. Phys. Chem. C* 2015, **119**, 12988–12998.
- 30 J. E. Sutton and D. G. Vlachos, *Ind. Eng. Chem. Res.* 2015, **54**, 4213–4225.
- 31 H. Li and G. Henkelman, *J. Phys. Chem. C* 2017, **121**, 27504–27510.
- 32 J. Courtois, W. Du, E. Wong, X. Teng, N. A. Deskins, *Appl. Catal. A-Gen.* 2014, **483**, 85–96.
- 33 R. Alcalá, M. Mavrikakis and J. A. Dumesic, *J. Catal.* 2003, **218**, 178–190.
- 34 T. Sheng, W. F. Lin and S. G. Sun, *Phys. Chem. Chem. Phys.* 2016, **18**, 15501–15504.
- 35 T. Sheng, W. F. Lin, C. Hardacre and P. Hu, *Phys. Chem. Chem. Phys.* 2014, **16**, 13248–13254.
- 36 X. Lu, Z. Deng, S. Wei, Q. Zhu, W. Wang, W. Guo and C. M. L. Wu, *Catal. Sci. Technol.* 2015, **5**, 3246–3258.
- 37 F. Studt, F. Abild-Pedersen, T. Bligaard, R. Sørensen, Z. C. H. Christensen and J. K. Nørskov, *Science*, 2008, **320**, 1320–1322.
- 38 M. Li, A. Kowal, K. Sasaki, N. Marinkovic, D. Su, E. Korach, P. Liu and R. R. Adzic, *Electrochimica Acta* 2010, **55**, 4331–4338.
- 39 Y. J. Kang, L. Qi, M. Li, R. E. Diaz, D. Su, R. R. Adzic, E. Stach, J. Li and C. B. Murray, *ACS Nano* 2012, **6**, 2818–2825.
- 40 S. Rudi, C. Cui, L. Gan and P. Strasser, *Electrocatalysis* 2014, **5**, 408–418.
- 41 M. Shao and R. R. Adzic, *Electrochim. Acta* 2005, **50**, 2415–2422.
- 42 Z. Y. Zhou, Q. Wang, J. L. Lin, N. Tian and S. G. Sun, *Electrochim. Acta* 2010, **55**, 7995–7999.
- 43 J. E. Sutton, P. Panagiotopoulou, X. E. Verykios and D. G. Vlachos, *J. Phys. Chem. C* 2013, **117**, 4691–4706.
- 44 H. F. Wang and Z. P. Liu, *J. Am. Chem. Soc.* 2008, **130**, 10996–11004.
- 45 A. A. Haleema and B. A. Alfred, *J. Electrochem. Soc.* 2015, **162**, F115–F122.
- 46 S. Linic, J. Jankowiak and M. A. Barteau, *J. Catal.* 2004, **224**, 489–493.
- 47 I. C. Man, H. Su, F. Calle-Vallejo, H. A. Hansen, J. I. Martínez, N. G. Inoglu, J. Kitchin, T. F. Jaramillo, J. K. Nørskov and J. Rossmeisl, *ChemCatChem* 2011, **3**, 1159–1165.
- 48 C. T. Campbell, *ACS Catal.* 2017, **7**, 2770–2779.
- 49 M. Mavrikakis, B. Hammer and J. K. Nørskov, *Phys. Rev. Lett.* 1998, **81**, 2819–2822.
- 50 J. Greeley, *Annu. Rev. Chem. Biomol. Eng.* 2016, **7**, 605–635.
- 51 A. Vojvodic and J. K. Nørskov, *Science* 2011, **334**, 1355–1356.
- 52 P. E. A. Tichi, *Phys. Rev B* 2006, **74**, 064202.
- 53 Z. W. Lu and B. M. Klein, *J. Phase Equilib.* 1995, **16**, 36–45.
- 54 M. Hansen and K. Anderko, *Constitution of Binary Alloys*, McGraw-Hill, New York or General Electric Co., Business Growth Services, Schenectady, New York (1958).
- 55 R. F. B. De Souza, L. S. Parreira, D. C. Rascio, J. C. M. Silva, E. Teixeira-Neto, M. L. Calegari, E. V. Spinace, A. O. Neto, M. C. Santos, *J. Power Sources* 2010, **195**, 1589–1593.
- 56 J. Greeley and M. Mavrikakis, *J. Am. Chem. Soc.* 2002, **124**, 7193–7201.
- 57 W. Zhong, Y. Liu and D. Zhang, *J. Phys. Chem. C* 2012, **116**, 2994–3000.
- 58 X. Lu, Z. Deng, C. Guo, W. Wang, S. Wei, S. P. Ng, X. Chen, N. Ding, W. Guo and C. M. L. Wu, *ACS Appl. Mater. Interfaces* 2016, **8**, 12194–12204.

- 59 C. Michel, F. Auneau, F. Delbecq and P. Sautet, *ACS Catal.* 2011, **1**, 1430–1440.
- 60 G. Kresse and J. Hafner, *Phys. Rev. B: Condens. Matter Mater. Phys.* 1993, **48**, 13115–13118.
- 61 G. Kresse and J. Furthmuller, *Phys. Rev. B: Condens. Matter Mater. Phys.* 1996, **54**, 11169–11186.
- 62 G. Kresse and J. Furthmuller, *Comput. Mater. Sci.* 1996, **6**, 15–50.
- 63 J. P. Perdew, K. Burke and M. Ernzerhof, *Phys. Rev. Lett.* 1996, **77**, 3865–3868.
- 64 P. E. Blochl, *Phys. Rev. B: Condens. Matter Mater. Phys.* 1994, **50**, 17953–17979.
- 65 G. Mills, H. Jonsson, G. K. Schenter, *Surf. Sci.* 1995, **324**, 305–337.
- 66 G. Henkelman and H. Jónsson, *J. Chem. Phys.* 2000, **113**, 9901–9904.
- 67 S. Maintz, V. L. Deringer, A. L. Tchougréeff and R. Dronskowski, *J. Comput. Chem.* 2013, **34**, 2557–2567.

View Article Online
DOI: 10.1039/C8TA03320J

TOC



There exists a volcano-shape composition-activity relationship for ternary Pt-Rh based nanoalloys towards ethanol electro-oxidation reaction.